Research Square

Preprints are preliminary reports that have not undergone peer review.
They should not be considered conclusive, used to inform clinical practice,
or referenced by the media as validated information.

The effect of heteroatoms on the formation of magnetic ceramic nanocomposites in pyrolysis of organometallic precursors: similar molecular structure, but totally different morphology, composition and properties

Zhijun Ruan (ruanzhijun87@126.com)
Huanggang Normal University https://orcid.org/0000-0001-9402-633X
Jingwen Ran
Huanggang Normal University
Shanshan Liu
Huanggang Normal University
Yanmei Chen
Huanggang Normal University
Xichao Wang
Huanggang Normal University
Jie Shi
Hefei University of Technology
Lihong Zhu
Huanggang Normal University
Shengfang Zhao
Huanggang Normal University
Junqi Lin
Huanggang Normal University

Research Article

Keywords: Organometallic precursors derived ceramics, Magnetic ceramic nanocomposites, Solid-state pyrolysis, Crystal phase

Posted Date: September 28th, 2020

DOI: https://doi.org/10.21203/rs.3.rs-81430/v1

License: This work is licensed under a Creative Commons Attribution 4.0 International License.
Read Full License

Abstract

Four organometallic compounds were synthesized for solid-state pyrolysis (SSP) to research the structure-property relationship between the precursors and the as-generated magnetic ceramic nanocomposites (MCNs). In which, the only saturated carbon atom in $\mathbf{M_C}$ was replaced by N or O or S atom, to produce $\mathbf{M_N}$, $\mathbf{M_O}$ and $\mathbf{M_S}$, respectively. It was found that, the crystal phase of the cobalt catalyst could be regulated by introducing different heteroatoms during the pyrolysis: fcc-Co for $\mathbf{M_C}$/$\mathbf{M_N}$, while fcc/hcp-Co hybrid for $\mathbf{M_O}$/$\mathbf{M_S}$. Metal cobalt with different crystal phases has their special catalytic and magnetic properties. Thus, MCNs with totally different morphology, composition and properties could be prepared by just changing one heteroatom in the precursors upon SSP. Uniform nanotubes were generated from pyrolysis of $\mathbf{M_C}$/$\mathbf{M_N}$, while nanospheres were generated from $\mathbf{M_O}$/$\mathbf{M_S}$. The obtained MCNs all show excellent magnetic properties with *Ms* ranged from 47.6 to 54.2 emu g^{-1}. Analyzing carefully, due to the magnetic difference between fcc-Co and hcp-Co, the *Ms* of the MCNs obtained from $\mathbf{M_O}$/$\mathbf{M_S}$ were slightly lower than those of $\mathbf{M_C}$/$\mathbf{M_N}$, but, their *Mr* and *Hc* were 2 to 5 times higher than the latter.

1. Introduction

Magnetic ceramic nanocomposites (MCNs) have attracted great attention due to their novel structure and unique properties for wide range of applications in various fields such as information storage [1, 2], catalysis [3, 4], microwave absorption [5, 6], environmental treatment [7, 8], and biomedical science [9, 10]. In MCNs, the magnetic nanoparticles well wrapped by the carbonaceous or other species, can possess excellent stability, dispersibility and biocompatibility [11, 12]. So far, various approaches have been successfully explored for the fabrication of functional MCNs, such as chemical vapor deposition, electric arc discharge, hydrothermal/solvothermal method and pyrolysis procedure *etc* [13–16]. And the prepared MCNs with different morphology and composition have their specific properties and application fields [17–20]. Although there are many fabrication methods for various MCNs, but controllable preparation of MCNs with desired morphology and properties is always a great challenge. More importantly, the growth mechanism of MCNs is still ambiguous.

Organometallic complexes containing both metal and carbon sources, are wonderful raw materials for the preparation of MCNs [21–26]. The metal-containing moieties could be transformed into metal nanoparticles under pyrolysis. Then, the generated metal catalyst could catalyze the formation of carbon nanoparticles (CNPs) [27–30]. Meanwhile, the magnetic metal NPs formed in the pyrolysis process could be well wrapped by the carbonaceous materials, to avoid their agglomeration and oxidation [31–34]. Recently, great achievements of Vollhardt and Müllen *et al*. demonstrated that solid-state pyrolysis (SSP) of organometallic complexes is a promising approach for the preparation of CNPs [35–38]. In SSP, powders of the organometallic precursors in quartz tubes were sealed under high vacuum, placed into a furnace underwent a stepwise thermolysis without the requirements for feedstock gases, inert atmosphere, extra catalyst, and expensive instruments. Especially, the well-defined organometallic precursors played a vital role in governing the structure and properties of the corresponding CNPs in SSP

[39–41]. In which, the structure of organic precursors could be subtly modified to control the morphology and the properties of the obtained CNPs. Thus, it is badly needed to know more about the structure-property relationship between the precursors and the products. Additionally, fewer experimental parameters in SSP provided favorable conditions for related research.

Therefore, to further research the structure-property relationship between the precursors and the as-generated MCNs, and explore the inherent mechanism, four organometallic compounds ($\mathbf{M_C}$~$\mathbf{M_S}$) with precise molecular structure were successfully synthesized for SSP. Surprisingly, just changing one heteroatom in the precursors could lead to totally different morphology, composition and properties of the as-generated MCNs (Fig. 1). After pyrolysis, the Co-containing moieties in $\mathbf{M_C}$/$\mathbf{M_N}$ were transformed into fcc-Co, but it was converted to fcc-Co/hcp-Co hybrid in $\mathbf{M_O}$/$\mathbf{M_S}$. Subsequently, morphology of the MCNs could be well controlled as nanotubes (for $\mathbf{M_C}$/$\mathbf{M_N}$) or nanospheres (for $\mathbf{M_O}$/$\mathbf{M_S}$) with adjustable size and magnetic properties. Experimental results indicated that heteroatom in the precursor could regulate the crystal phase of metal Co, and the crystal phase greatly affect the catalyst activities and magnetic properties of Co, thereby controlling the morphology and properties of the resultant MCNs upon SSP. The result once again confirmed the power of the concept of precursor-controlled pyrolysis towards defined MCNs, and provided valuable rules and guidance for the controllable preparation of MCNs.

2. Experimental

2.1 Material

Octacarbonyldicobalt ($Co_2(CO)_8$) was purchased from Alfa Aesar. Dichloromethane (DCM) was dried over and distilled from CaH_2. Tetrahydrofuran (THF) was distilled from K-Na alloy under dry nitrogen. Compounds **1**–**4** were synthesized according to previous literatures. All other reagents were used as received without further purification.

2.2 Synthesis of the organometallic compounds

General procedure for the synthesis of organometallic compounds $\mathbf{M_C}$, $\mathbf{M_N}$, $\mathbf{M_O}$ and $\mathbf{M_S}$: $Co_2(CO)_8$ (6.00 equiv) and compound **1** or **2** or **3** or **4** (1.00 equiv) were dissolved in THF under an argon atmosphere. The mixture was stirred overnight at room temperature and the solvent was removed under vacuum. The residue was purified by using column chromatography on neutral Al_2O_3 with DCM-petroleum ether mixture as the eluent.

Compound M_C: Black solid was obtained in 68% yield. ^{1}H NMR (300 MHz, $CDCl_3$) δ (ppm): 7.78 (m, 4H, ArH), 7.65 (m, 6H, ArH), 7.39 (m, 6H, ArH), 3.98 (s, 2H, -CH2-). ^{13}C NMR (100 MHz, $CDCl_3$) δ (ppm): 199.5, 144.5, 141.4, 138.6, 137.3, 129.4, 129.2, 128.7, 128.1, 125.8, 120.6, 92.5, 92.4, 36.9. FTIR (thin film), ν (cm^{-1}): 2016.2, 2052.4, 2088.6 ($Co_2(CO)_6$). Anal. calcd for $C_{41}H_{18}Co_4O_{12}$: C 52.48, H 1.93; found: C 52.93, H 2.11.

Compound M_N: Black solid was obtained in 80% yield. ^{1}H NMR (300 MHz, $CDCl_3$) δ (ppm): 8.32 (br, 3H, ArH), 7.64 (br, 6H, ArH), 7.39 (br, 8H, ArH). ^{13}C NMR (100 MHz, $CDCl_3$) δ (ppm): 199.6, 139.8, 138.9, 129.8, 129.4, 129.1, 128.3, 127.9, 123.6, 121.2, 93.5, 92.3. FTIR (thin film), ν (cm^{-1}): 2018.0, 2050.6, 2088.6 ($Co_2(CO)_6$), 3409.5 (N-H). Anal. calcd for $C_{40}H_{17}Co_4NO_{12}$: C 51.15, H 1.82, N 1.49; found: C 52.03, H 1.74, N 1.57.

Compound M_O: Black solid was obtained in 76% yield. ^{1}H NMR (300 MHz, $CDCl_3$) δ (ppm): 8.15 (s, 2H, ArH), 7.54 (d, J = 8.4 Hz, 2H, ArH), 7.63 (m, 6H, ArH), 7.38 (m, 6H, ArH). ^{13}C NMR (100 MHz, $CDCl_3$) δ (ppm): 199.6, 156.6, 138.5, 133.6, 129.5, 129.4, 129.2, 128.2, 124.6, 121.1, 92.3, 91.9. FTIR (thin film), ν (cm^{-1}): 2019.8, 2051.1, 2089.5 ($Co_2(CO)_6$). Anal. calcd for $C_{40}H_{16}Co_4O_{13}$: C 51.09, H 1.72; found: C 51.69, H 1.61.

Compound M_S: Black solid was obtained in 65% yield. ^{1}H NMR (300 MHz, $CDCl_3$) δ (ppm): 8.36 (s, 2H, ArH), 7.85 (d, J = 8.1 Hz, 2H, ArH), 7.65 (m, 6H, ArH), 7.36 (m, 6H, ArH). ^{13}C NMR (75 MHz, $CDCl_3$) δ (ppm): 199.4, 139.8, 138.5, 136.0, 135.5, 129.3, 128.7, 128.2, 128.0, 123.6, 122.6, 92.5, 91.8. FTIR (thin film), ν (cm^{-1}): 2019.6, 2051.5, 2088.5 ($Co_2(CO)_6$). Anal. calcd for $C_{40}H_{16}Co_4O_{12}S$: C 50.24, H 1.69; found: C 50.86, H 1.51.

2.3 Instrumentation

^{1}H and ^{13}C NMR spectroscopy study was conducted with a Varian Mercury 300 spectrometer and 400 MHz Bruker Avance NMR spectrometer using tetramethylsilane (TMS; δ = 0 ppm) as internal standard. EI-MS spectra were recorded with a Finnigan PRACE mass spectrometer. Elemental analyses were performed by a CARLOERBA-1106 by a micro-elemental analyzer. The Fourier transform infrared (FTIR) spectra were recorded on a PerkinElmer-2 spectrometer in the region of 4000 – 400 cm^{-1}. Thermogravimetric analysis (TGA) was performed on Netzsch STA 449C thermal analyzer at a heating rate of 10 ^oC/min in nitrogen at a flow rate of 20 cm^3/min. Scanning electron microscopy (SEM) was performed on a ZEISS-SIGMA scanning electron microscope. Transmission electron microscopy (TEM) was performed on a JEM-2010HT or JEM-2010FEF microscope at an accelerating voltage of 200 kV. TEM samples were prepared by drying a droplet of the suspension on a TEM copper grid with a carbon film. Energy-dispersive X-ray spectroscopy (EDX) was taken on the SEM or TEM. The X-ray diffraction (XRD) analyses were performed on a Bruker D8 Advanced X-ray diffractometer with CuKα radiation (λ = 1.5418 Å). Magnetization curves were recorded on a physical property measurement system (PPMS-9T) with a vibrating sample magnetometer (VSM) option at room temperature.

3. Results And Discussion

3.1. Synthesis and characterization

M $_C$ was synthesized with fluorene as the basic unit. Then, replacing the only saturated carbon atom in **M**$_C$ with nitrogen (or oxygen or sulfur) atom, **M**$_N$, **M**$_O$ and **M**$_S$ were obtained, respectively. Scheme S1 illustrates the synthetic routes to the intermediates and final products. Firstly, alkynyl-functionalized compounds **1** ~ **4** were synthesized by the palladium-catalyzed Sonogashira coupling reaction. Then, organometallic compounds **M**$_C$, **M**$_N$, **M**$_O$ and **M**$_S$ were all prepared via the reaction between the alkynyl-functionalized intermediates (**1** ~ **4**) and an excess of $Co_2(CO)_8$, affording [$CCCo_2(CO)_6$] moieties with a satisfactory yield. All the compounds were well characterized by nuclear magnetic resonance (NMR), mass spectroscopy, elemental analysis (EA), and Fourier transform infrared (FTIR) spectroscopy, which well confirmed their explicit molecular structures (Fig. S7-S22).

Figure 2 shows the IR spectra of **1**, **2**, **M**$_C$ and **M**$_N$. The stretching vibration of the alkynyl groups of **1** and **2** appeared at about 2210 cm^{-1}, which completely disappeared in the spectra of **M**$_C$ and **M**$_N$. However, in the spectra of **M**$_C$ and **M**$_N$, three strong absorption bands appeared in the range of 2010 to 2090 cm^{-1}, which were the typical absorptions of [$CCCo_2(CO)_6$], confirming that alkynyl group has been completely reacted with the $Co_2(CO)_8$ [42]. Meanwhile, due to the presence of the N-H bond in **2** and **M**$_N$, they also showed an absorption peak at about 3400 cm^{-1}. The IR spectra of all the organometallic compounds and the intermediates are given in Fig. S1, and similar results were obtained. Figure 3 shows the ^{1}H NMR and ^{13}C NMR spectra of **3** and **M**$_O$. After incorporation with the [$Co_2(CO)_6$] unit, the ^{13}C NMR spectra demonstrated obvious signal shift for the carbons of the alkynyl group. The signal assigned to the C ≡ C (Ca) shifted from 89.4/89.9 to 91.9/92.3 ppm (Ca'). In addition, a strong singlet assigned to the carbonyl carbon (Cb) of [$CCCo_2(CO)_6$] was appeared at about 199.4 ppm [43]. Moreover, for both ^{1}H NMR and ^{13}C NMR spectra, great changes had also taken place in the aromatic areas that close to the [$CCCo_2(CO)_6$] unit.

3.2 Thermal properties and pyrolysis process

In SSP, the samples would undergo a stepwise thermolysis program: they were first heated to their decomposition temperature of the metal carbonyl groups and held at this temperature for several hours, then heated to a higher temperature and held there for another several hours. Thus, the thermal properties of the organometallic compounds were investigated by using TGA. The thermal-decomposition temperatures (T_d, corresponding to 5% weight loss) of the precursors were at about 170 ^oC (Fig. S2). Thus, the pyrolysis program was determined as following: powders of the organometallic precursors in quartz tubes were sealed under high vacuum, and then placed into one furnace, and underwent exactly the same heating programs. The samples were first heated to 170 °C with a rate of 2 ^oC/min, held for 2 h, and then heated to a higher temperature (700 ^oC) with a rate of 5 ^oC/min, held for 8 h. After cooling to room temperature, the obtained products were characterized by scanning electron microscopy (SEM), transmission electron microscopy (TEM), energy-dispersive spectroscopy (EDX), powder X-ray diffraction (XRD) and vibrating sample magnetometer (VSM).

3.3 Morphological characterization of the MCNs

As discussed above, it is a powerful approach to yield defined CNPs through the precursor-controlled pyrolysis process. Actually, the prepared organometallic compounds could be well converted to two types of MCNs, nanotubes and nanospheres, under the same pyrolysis program with high yield. Upon the SSP process, $\mathbf{M_C}$ and $\mathbf{M_N}$ produced uniform multiwalled CNTs in high yields (Fig. 4a-f). TEM analysis revealed that the average inner and outer diameters of the CNTs were about 20 and 40 nm for $\mathbf{M_C}$, respectively (Fig. 4b). And the length of these CNTs was above 10 μm. From the high-resolution TEM (HRTEM) image, the nanotubes were well graphitized, made up of ~ 25 layers, and the space between the layers was 3.51 Å (Fig. 4c and S3a), in consistency with the range (d_{002} = 0.34–0.39 nm) reported for the interplanar spacings of graphite [44]. Co NPs having a diameter of 15–50 nm, were located mainly at the tip of the CNTs and wrapped in orderly graphene layers (Fig. 5a and S3b) or encapsulated by well graphitized carbon nanospheres. As to the precursor $\mathbf{M_N}$, CNTs with reduced length (< 1 μm) but increased diameter were obtained. The as-prepared CNTs had a uniform size with an inner diameter about 30 nm and an outer diameter about 60 nm (Fig. 4d, e), 1.5 times of the size of the CNTs obtained from $\mathbf{M_C}$, and the wall of the CNTs was comprised of 40 graphene layers with d_{002} = 3.47 Å (Fig. 4f). As shown in Fig. 5b and S3d, the top of the CNT clearly demonstrated its multilayer tubular structure.

Surprisingly, unlike the cases of $\mathbf{M_C}$ and $\mathbf{M_N}$, MCNs with totally different morphology were obtained as just changing one heteroatom in the precursors (from N to O or S). SSP of $\mathbf{M_O}$ and $\mathbf{M_S}$, both gave uniform nanospheres with a Co@C core-shell structure. For $\mathbf{M_O}$, SEM and TEM analysis showed that the diameter of the formed nanospheres was mainly about 10–15 nm (Fig. 4g-i). And the Co NPs were well embedded in amorphous carbon and graphitized carbon with a thickness of 5–10 nm. As showed in Fig. 5c and S4, Co NPs was well embedded in graphitized carbon (d_{002} = 3.43 Å), and its lattice structure was very clear. The spacing between the lattice planes was, respectively, 0.174 nm and 0.216 nm corresponding to the (111) planes of face centered cubic (fcc) and (100) planes of hexagonal-closed-packed (hcp) phases of cobalt [45, 46], illustrating the coexistence of the fcc (bule area in Fig. 5c) and the hcp (gree area) structures. And, the fcc phase locating at the center was surrounded by the hcp phase.

As to precursor $\mathbf{M_S}$, SEM and TEM analysis showed that the diameter of the nanospheres mainly ranged from 35 to 55 nm, and Co NPs were encapsulated very well in carbonaceous materials (Fig. 4j-l). And the lattice fringes of Co could be clearly observed through the HRTEM image (Fig. 4l). Interestingly, a special phenomenon was observed in the case of precursor $\mathbf{M_S}$: cobalt core/carbon sheath nanocable with diameter of about 200 nm and length of 7 μm was obtained (Fig. 5d and S5). TEM-EDX was used to analyze the element distribution of the nanocable (Fig. 5e). When the electron beam passed through the core (label 1–1 in Fig. 5d) and the sheath (label 1–2) of the nanocable, Co and C were the main elements detected (Cu was come from the copper grid), confirming its cobalt core/carbon sheath architecture.

It is amazing how does the changing of just one atom leads to the formation of MCNs with totally different morphology? Generally, fcc and hcp are the two main different crystalline structures of cobalt.

Among them, the hcp-Co is stable at room temperature, while the fcc-Co is a metastable phase formed at temperature above 450 °C [47]. In pyrolysis, the heating temperature was generally higher than 500 °C, so cobalt mainly existed in the fcc phase, especially for the production of CNTs [48, 49]. Although, cobalt is a very common catalyst for the synthesis of CNTs, and the morphology, density and size effect of Co have been extensively studied [50–53]. However, the impact of the crystal phase was rarely considered, mainly because of the absence of the room temperature stable hcp phase (transformation to high temperature stable fcc phase) during the pyrolysis under high temperature. On the other hand, even though hcp-Co could exist under some special conditions in pyrolysis, but their main pyrolysis products were carbon-encapsulated cobalt NPs without CNTs [54–56]. These results indicated that, fcc-Co was a better active catalyst phase for the fabrication of CNTs, while hcp-Co was conducive to the generation of carbon-encapsulated cobalt NPs.

Very importantly, in the classic cobalt-catalyzed Fischer-Tropsch reaction, great achievements have demonstrated that hcp-Co has better catalytic activity than fcc-Co [57, 58]. This is mainly due to the special surface structure of the hcp crystal phase, which has higher intrinsic activity and density of active sites. So it is more beneficial to the decomposition, diffusion and recombination of carbon source on its surface [59]. Similarly, during the catalytic pyrolysis, the hydrocarbons carbon source was first absorbed and decomposed by the catalyst, and then diffused and restructured into shaped CNPs [60, 61]. Thus, based on the experimental results and inspired by the above mechanism, it was speculated that the excessively fast diffusion and deposition rate of the carbon source on hcp-Co would cause the completely encapsulation of cobalt NPs by carbon (formation of cobalt core-carbon shell NPs), which was not favoring to the nucleation and growth of the CNTs. On the contrary, the moderate catalytic activity of fcc-Co could contribute to the gradual nucleation and growth of CNTs. The exact mechanism was unclear, further research was still needed to better understand this interesting phenomenon. However, in this work, for the first time, we found that heteroatom (even just changing one atom) in the organometallic precursor could regulate the crystal phase of metal Co, thereby controlling the morphology the resultant MCNs upon SSP, providing an effective approach to prepare MCNs controllably.

3.4 Composition of the MCNs

Powder XRD was used to further investigate the crystal phase of the produced MCNs. To differentiate the pyrolysis products from their precursors, the MCNs obtained from $\mathbf{M_C}$, $\mathbf{M_N}$, $\mathbf{M_O}$ and $\mathbf{M_S}$ were named as $\mathbf{M_C}$-S, $\mathbf{M_N}$-S, $\mathbf{M_O}$-S and $\mathbf{M_S}$-S, respectively. Figure 6 shows the XRD patterns of the synthesized nanocomposites. $\mathbf{M_C}$-S and $\mathbf{M_N}$-S exhibited Bragg reflections at 2θ angles of 44.3, 51.6 and 75.9^o, which could be identified to be the (111), (200) and (220) planes of the fcc-Co structure [62]. And, due to the presence of metallic cobalt and other impurities covering on the as-synthesized CNTs, diffraction peak at about 26^o that correspond to the (002) plane of graphite structure was very weak [63, 64]. As expected, just like the result found via HRTEM, as to $\mathbf{M_O}$-S and $\mathbf{M_S}$-S, in addition to the fcc phase, peaks at 41.6^o and 47.5^o that correspond to (100) and (101) planes of the hcp phase also appeared, indicating the coexistence of fcc/hcp phase [65]. Meanwhile, in comparison with those of $\mathbf{M_O}$-S, the intensity of the

diffraction peaks for hcp phase in **M_S-S**, became much narrower and sharper, indicating an improvement in crystallinity and enlargement of the cobalt nanocrystallite size [66]. SEM-EDX was used to analyze the chemical compositions of the obtained nanocomposites. From the EDX results, except a small amount of sulfur existing in **M_S-S**, the main compositions of all the MCNs that could be detected were Co and C elements, and the cobalt contents were about 30% (Fig. S6).

3.5 Magnetism of the MCNs

All the Co enriched nanocomposites were magnetizable and could be quickly attracted to a magnet at room temperature. Thus, to further research the magnetism of the obtained MCNs, especially highlight the impact of hcp-Co on the magnetic anisotropy, VSM was utilized to quantificationally investigate their magnetic properties at a temperature of 300 K. Figure 7 shows the magnetization curves of the MCNs, all the samples exhibited soft ferromagnetic behavior with high magnetizability. The magnetization rapidly increased with an increase in the strength of the applied field before 5 kOe, with relatively low magnetic remanence (*Mr*) and coercivity (*Hc*). The magnetization data were summarized in Table 1, the saturation magnetization (*Ms*) of the produced MCNs ranged from 47.6 to 54.2 emu g^{-1}, showing good magnetic properties. Analyzing carefully, the *Ms* of the MCNs obtained from **M_O/M_S** were slightly lower than those of **M_C/M_N**, but, their *Mr* and *Hc* were 2 to 5 times higher than the latter. The *Ms* and *Hc* of **M_C-S/M_N-S** were 6.8/5.9 emu g^{-1} and 150/190 Oe, respectively. However, as to **M_O-S/M_S-S**, these values significantly increased to 12.6/14.2 emu g^{-1} and 760/610 Oe, respectively. Considering the presence of hcp-Co, this result is understandable: comparing with fcc-Co, hcp-Co has a slightly lower *Ms*, but with much stronger *Ms* and *Hc* [67, 68]. Therefore, the hcp-Co generated in **M_O-S/M_S-S**, leaded to a significant magnetic difference of the prepared MCNs.

Table 1
Magnetization data for various samples measured at 300 K

sample	*Ms* (emu/g)	*Mr* (emu/g)	*Mr*/*Ms*	Hc (Oe)
M_C-S	54.5	6.8	0.12	150
M_N-S	51.7	5.9	0.11	190
M_O-S	50.6	12.6	0.25	760
M_S-S	47.6	14.2	0.30	610

4. Conclusion

In conclusion, through rational molecular design, four organometallic precursors were synthesized successfully for solid-state pyrolysis (SSP) to research the structure-property relationship between the precursors and the as-generated MCNs. It was found that, the crystal phase of the cobalt catalyst could be regulated by introducing different heteroatoms, and the crystal phase greatly affect the catalyst

activities and magnetic properties of Co, thereby controlling the morphology, composition and magnetic properties of the resultant MCNs upon SSP. By simply changing one heteroatom in the precursors, uniform nanotubes and nanospheres with adjustable size and magnetic properties could be controllably prepared efficiently with high selectivity. The obtained MCNs all show excellent and differential magnetic properties. Coupled with their high oxidation resistance and good stability, they could be promising candidates in practical magnetic and catalytic applications. Thus, the preliminary results confirmed the power of the precursor-controlled SSP, and also provided valuable guidance for the controllable preparation and the mechanism research of MCNs.

5. Declarations

Declaration of competing interest

The authors declared that they have no conflicts of interest to this work.

Acknowledgements

We are grateful to the National Natural Science Foundation of China (21704032, 21501061), Natural Science Foundation of Hubei Province (2017CFB223), Research Foundation of Huanggang Normal University (201721703, 201721903) for financial support.

6. References

1. Sun S, Murray CB, Weller D et al (2000) Monodisperse FePt nanoparticles and ferromagnetic FePt nanocrystal superlattices. Science 287:1989–1992
2. Dong Q, Li G, Ho CL et al (2012) A polyferroplatinyne precursor for the rapid fabrication of $L1_0$-FePt-type bit patterned media by nanoimprint lithography. Adv Mater 24:1034–1040
3. Kainz QM, Reiser OL (2014) Polymer- and dendrimer-coated magnetic nanoparticles as versatile supports for catalysts, scavengers, and reagents. Acc Chem Res 47:667–677
4. Wang D, Astruc D (2014) Fast-growing field of magnetically recyclable nanocatalysts. Chem Rev 114:6949–6985
5. Liu T, Pang Y, Zhu M et al (2014) Microporous Co@CoO nanoparticles with superior microwave absorption properties. Nanoscale 6:2447–2454
6. Liu T, Xie X, Pang Y et al (2016) Co/C nanoparticles with low graphitization degree: a high performance microwave-absorbing material. J Mater Chem C 4:1727–1735
7. Wu Z, Li W, Webley PA et al (2012) General and controllable synthesis of novel mesoporous magnetic iron oxide@carbon encapsulates for efficient arsenic removal. Adv Mater 24:485–491
8. Gómez-Pastora J, Bringas E, Ortiz I (2014) Recent progress and future challenges on the use of high performance magnetic nano-adsorbents in environmental applications. Chem Eng J 256:187–204

9. Seo WS, Lee JH, Sun XM et al (2006) FeCo/graphitic-shell nanocrystals as advanced magnetic-resonance-imaging and near-infrared agents. Nat Mater 5:971–976
10. Oh WK, Yoon H, Jang J (2010) Size control of magnetic carbon nanoparticles for drug delivery. Biomaterials 31:1342–1348
11. Zhu M, Diao G (2011) Review on the progress in synthesis and application of magnetic carbon nanocomposites. Nanoscale 3:2748–2767
12. Lu AH, Salabas EL, Schüth F (2007) Magnetic nanoparticles: synthesis, protection, functionalization, and application. Angew Chem Int Ed 46:1222–1244
13. Kong J, Cassell AM, Dai H (1998) Chemical vapor deposition of methane for single-walled carbon nanotubes. Chem Phys Lett 292:567–574
14. Qi XS, Qin C, Zhong W et al (2010) Large-scale synthesis of carbon nanomaterials by catalytic chemical vapor deposition: A review of the effects of synthesis parameters and magnetic properties. Materials 3:4142–4174
15. Siddiqui MTH, Nizamuddin S, Baloch HA et al (2018) Synthesis of magnetic carbon nanocomposites by hydrothermal carbonization and pyrolysis. Environ Chem Lett 16:821–844
16. Dong Q, Meng Z, Ho CL et al (2018) A molecular approach to magnetic metallic nanostructures from metallopolymer precursors. Chem Soc Rev 47:4934–4953
17. Reddy LH, Arias JL, Nicolas J et al (2012) Magnetic nanoparticles: design and characterization, toxicity and biocompatibility, pharmaceutical and biomedical applications. Chem Rev 112:5818–5878
18. Zhang Q, Yang X, Guan J (2019) Applications of magnetic nanomaterials in heterogeneous catalysis. ACS Appl Nano Mater 2:4681–4697
19. Yang Z, Yang N, Yang J et al (2014) Control of the oxygen and cobalt atoms diffusion through Co nanoparticles differing by their crystalline structure and size. Adv Funct Mater 25:891–897
20. Ye F, Dai H, Peng K et al (2020) Effect of Mn doping on the microstructure and magnetic properties of $CuFeO_2$ ceramics. J Adv Ceram 9:444–453
21. Abd-El-Aziz AS, Shipman PO, Boden BN et al (2010) Synthetic methodologies and properties of organometallic and coordination macromolecules. Prog Polym Sci 35:714–836
22. Li H, Li L, Wu H et al (2013) Ferrocene-based poly (aroxycarbonyltriazole)s: synthesis by metal-free click polymerization and use as precursors to magnetic ceramics. Polym Chem 4:5537–5541
23. AL-Badri ZM, Maddikeri RR, Zha Y et al (2011) Room temperature magnetic materials from nanostructured diblock copolymers. Nat Commun 2:482
24. Jiang B, Hom WL, Chen X et al (2016) Magnetic hydrogels from alkyne/cobalt carbonyl-functionalized ABA triblock copolymers. J Am Chem Soc 138:4616–4625
25. Yu Z, Yang L, Min H et al (2014) Single-source-precursor synthesis of high temperature stable SiC/C/Fe nanocomposites from a processable hyperbranched polyferrocenylcarbosilane with high ceramic yield. J Mater Chem C 2:1057–1067

26. Meng Z, Li G, Yiu SC et al (2020) Nanoimprint lithography-directed self-assembly of bimetallic iron-M (M = Palladium, Platinum) complexes for magnetic patterning. Angew Chem Int Ed 59:11521–11526
27. Whittell GR, Manners I (2007) Metallopolymers: new multifunctional materials. Adv Mater 19:3439–3468
28. Nyamori VO, Mhlanga SD, Coville NJ (2008) The use of organometallic transition metal complexes in the synthesis of shaped carbon nanomaterials. J Organomet Chem 693:2205–2222
29. Ruan Z, Zhang Y, Tu J et al (2016) Dramatically enhancing the yield of carbon nanotubes by simply adding oxygen-containing molecules in solid-state synthesis. Chem Commun 52:2976–2979
30. Wen Q, Yu Z, Riedel R (2020) The fate and role of in situ formed carbon in polymer-derived ceramics. Prog Mater Sci 109:100623
31. Zalich MA, Baranauskas VV, Riffle JS et al (2006) Structural and magnetic properties of oxidatively stable cobalt nanoparticles encapsulated in graphite shells. Chem Mater 18:2648–2655
32. Ruan Z, Qin J, Li Z (2015) The partially controllable growth trend of carbon nanoparticles in solid-state pyrolysis of organometallic precursor by introducing POSS units, and their magnetic properties. RSC Adv 5:63296–63303
33. Ruan Z, Rong W, Li Q et al (2015) Synthesis and solid-state pyrolysis behavior of POSS containing organometallic polymer with dicobalt hexacarbonyl in the side chain. J Inorg Organomet Polym 25:98–106
34. Ruan Z, Rong W, Zhan X et al (2014) POSS containing organometallic polymers: synthesis, characterization and solid-state pyrolysis behavior. Polym Chem 5:5994–6002
35. Dosa PI, Erben C, Iyer VS et al (1999) Metal encapsulating carbon nanostructures from oligoalkyne metal complexes. J Am Chem Soc 121:10430–10431
36. Wu J, Hamaoui BE, Li J et al (2005) Solid-state synthesis of “bamboo-like” and straight carbon nanotubes by thermolysis of hexa-peri-hexabenzocoronene-cobalt complexes. Small 1:210–212
37. Hamaoui BE, Zhi L, Kolb U et al (2005) Uniform carbon and carbon/cobalt nanostructures by solid-state thermolysis of polyphenylene dendrimer/cobalt complexes. Adv Mater 17:2957–2960
38. Zhi L, Hu YS, Hamaoui BE et al (2008) Precursor-controlled formation of novel carbon/metal and carbon/metal oxide nanocomposites. Adv Mater 20:1727–1731
39. Hamaoui BE, Zhi L, Wu J et al (2007) Solid-state pyrolysis of polyphenylene-metal complexes: a facile approach toward carbon nanoparticles. Adv Funct Mater 17:1179–1187
40. Ruan Z, Rong W, Li Q et al (2015) Oxygen as the growth enhancer of carbon nanotubes in solid-state pyrolysis of organometallic precursors. Carbon 87:338–346
41. Ruan Z, Li Z (2020) Recent progress of magnetic nanomaterials from cobalt-containing organometallic polymer precursors. Polym Chem 11:764–778
42. Constable EC, Eich O, Fenske D et al (2000) Metallostars: high-nuclearity linearly developed nanostructures containing multiple cluster motifs. Chem Eur J 6:4364–4370

43. Wilson JL, Kobeissi SF, Oudir S et al (2014) Design and synthesis of new hybrid molecules that activate the transcription factor Nrf2 and simultaneously release carbon monoxide. Chem Eur J 20:14698–14704
44. Kiang CH, Endo M, Ajayan PM et al (1998) Size effects in carbon nanotubes. Phys Rev Lett 81:1869–1872
45. Tyagi PK, Misra A, Singh MK et al (2005) High-resolution transmission electron microscopy mapping of nickel and cobalt single-crystalline nanorods inside multiwalled carbon nanotubes and chirality calculations. Appl Phys Lett 86:253110
46. Kotoulas A, Dendrinou-Samara C, Sarafidis C et al (2017) Carbon-encapsulated cobalt nanoparticles: synthesis, properties, and magnetic particle hyperthermia efficiency. J Nanopart Res 19:399
47. O'Shea VA, Moreira I, Roldán A et al (2010) Electronic and magnetic structure of bulk cobalt: The α, β, and ε-phases from density functional theory calculations. J Chem Phys 133:024701
48. Iyer VS, Vollhardt KPC, Wilhelm R (2003) Near-quantitative solid-state synthesis of carbon nanotubes from homogeneous diphenylethynecobalt and-nickel complexes. Angew Chem Int Ed 42:4379–4383
49. Ruan Z, Chan CYK, Lam JWY et al (2014) Controllable preparation of nanocomposites through convenient structural modification of cobalt contained organometallic precursors: nanotubes and nanospheres with high selectivity, and their magnetic properties. J Mater Chem C 2:633–640
50. Nyamori VO, Coville NJ (2007) Effect of ferrocene/carbon ratio on the size and shape of carbon nanotubes and microspheres. Organometallics 26:4083–4085
51. Huh Y, Green MLH, Kim YH et al (2005) Control of carbon nanotube growth using cobalt nanoparticles as catalyst. Appl Surf Sci 249:145–150
52. Kumar M, Ando Y (2010) Chemical Vapor Deposition of Carbon Nanotubes: A Review on Growth Mechanism and Mass Production. J Nanosci Nanotechnol 10:3739–3758
53. Bedewy M, Meshot ER, Hart AJ (2012) Diameter-dependent kinetics of activation and deactivation in carbon nanotube population growth. Carbon 50:5106–5116
54. O'Shea VA, Piscina PR, Homs N et al (2009) Development of hexagonal closed-packed cobalt nanoparticles stable at high temperature. Chem Mater 21:5637–5643
55. Zhu W, Ren J, Gu X et al (2011) Synthesis of hermetically-sealed graphite-encapsulate metallic cobalt (alloy) core/shell nanostructures. Carbon 49:1461–1472
56. Kumar R, Manjunatha M, Anupama AV et al (2019) Synthesis, composition and spin-dynamics of FCC and HCP phases of pyrolysis derived Co-nanoparticles embedded in amorphous carbon matrix. Ceram Int 45:19879–19887
57. Liu JX, Su HY, Sun DP et al (2013) Crystallographic dependence of CO activation on cobalt catalysts: hcp versus fcc. J Am Chem Soc 135:16284–16287
58. Tsakoumis NE, Patanou E, Lögdberg S et al (2019) Structure-performance relationships on Co-based Fischer-Tropsch synthesis catalysts: the more defect-free, the better. ACS Catal 9:511–520

59. Liu S, Li Y, Shen W (2015) Tuning the catalytic behavior of metal nanoparticles: The issue of the crystal phase. Chin J Catal 36:1409–1418
60. Jourdain V, Bichara C (2013) Current understanding of the growth of carbon nanotubes in catalytic chemical vapour deposition. Carbon 58:2–39
61. Page AJ, Ohta Y, Irle S et al (2010) Mechanisms of single-walled carbon nanotube nucleation, growth, and healing determined using QM/MD methods. Acc Chem Res 43:1375–1385
62. Liu S, Tang X, Yin L et al (2000) Synthesis of carbon nanoflasks. J Mater Chem 10:1271–1272
63. Huang H, Yang S, Gu G (1998) Preparation of carbon-coated cobalt nanocrystals in a new gas blow arc reactor and their characterization. J Phys Chem B 102:3420–3424
64. Liu S, Zhu J, Mastai Y et al (2000) Preparation and characteristics of carbon nanotubes filled with cobalt. Chem Mater 12:2205–2211
65. He Q, Yuan T, Zhang X et al (2013) Magnetically soft and hard polypropylene/cobalt nanocomposites: role of maleic anhydride grafted polypropylene. Macromolecules 46:2357–2368
66. Ennas G, Falqui A, Marras S et al (2004) Influence of metal content on size, dispersion, and magnetic properties of iron-cobalt alloy nanoparticles embedded in silica matrix. Chem Mater 16:5659–5663
67. Doi K, Minamitani E, Yamamoto S et al (2015) Electronic and magnetic effects of a stacking fault in cobalt nanoscale islands on the Ag(111) surface. Phys Rev B 92:064421
68. Ritter U, Scharff P, Grechnev GE et al (2011) Structure and magnetic properties of multi-walled carbon nanotubes modified with cobalt. Carbon 49:4443–4448

Figures

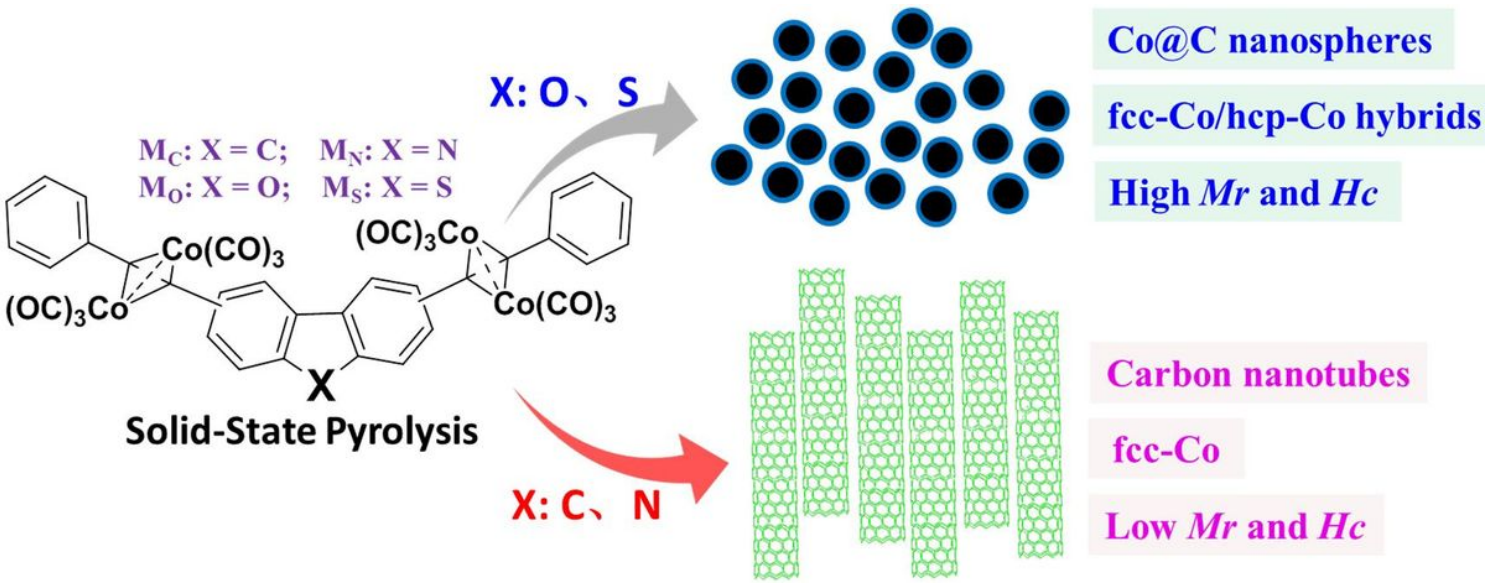


Figure 1

Chemical structure of compounds MC~MS, and the as-generated magnetic nanocomposites with different morphology, composition and properties.

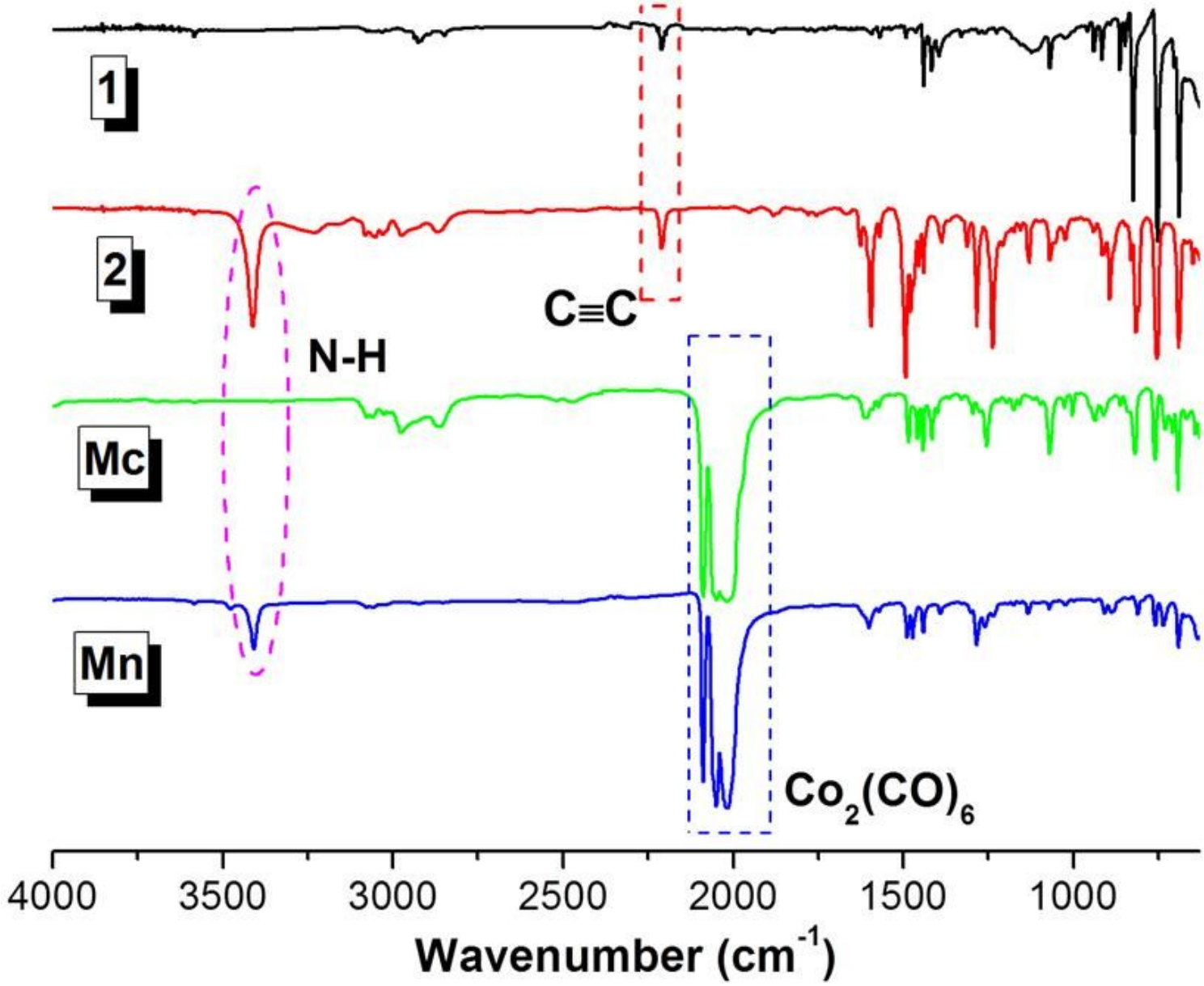


Figure 2

IR spectra of compounds 1, 2 and organometallic precursors MC, MN.

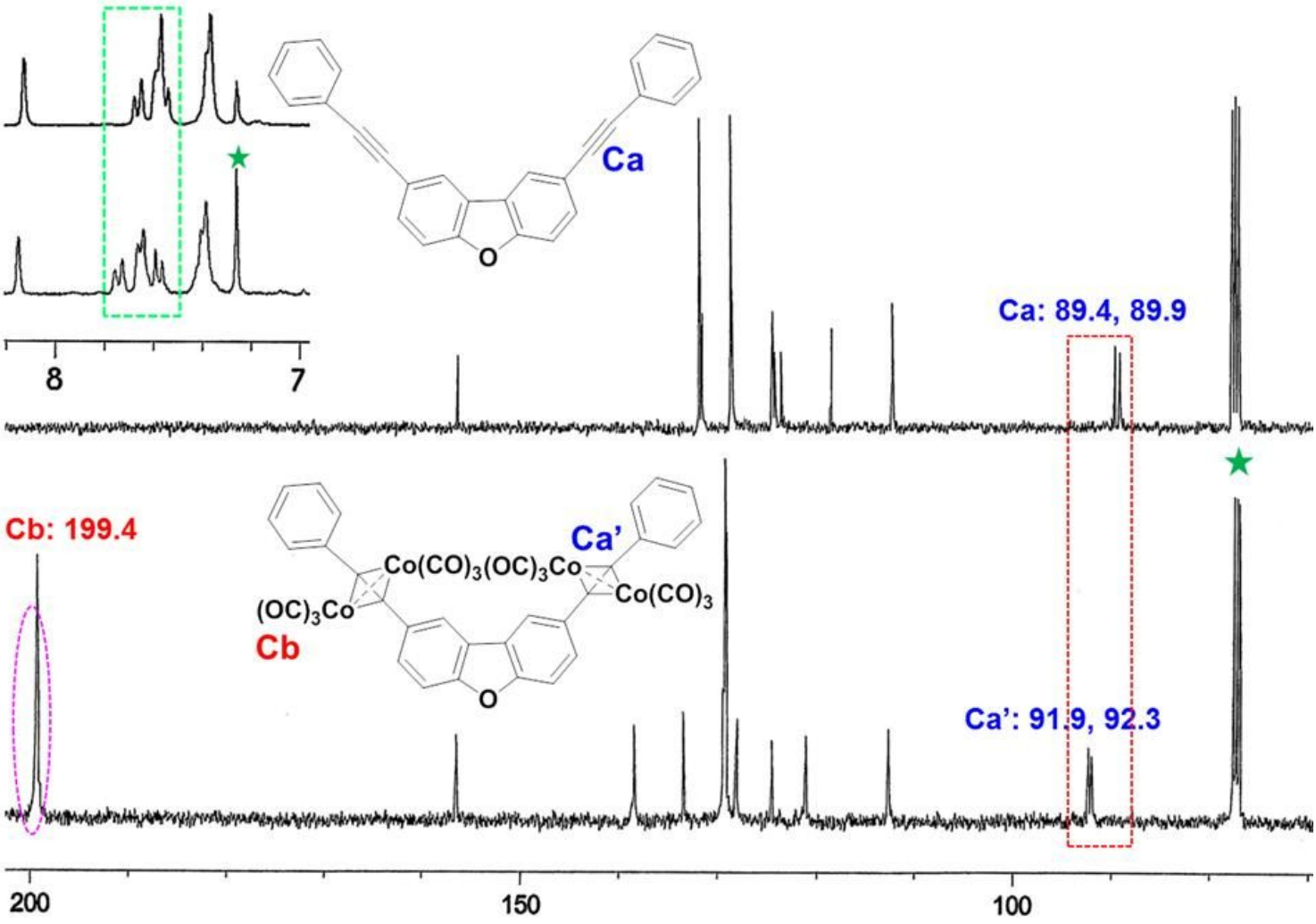


Figure 3

1H NMR and 13C NMR spectra of 3 and MO (in CDCl3), the solvent peaks are marked with asterisks.

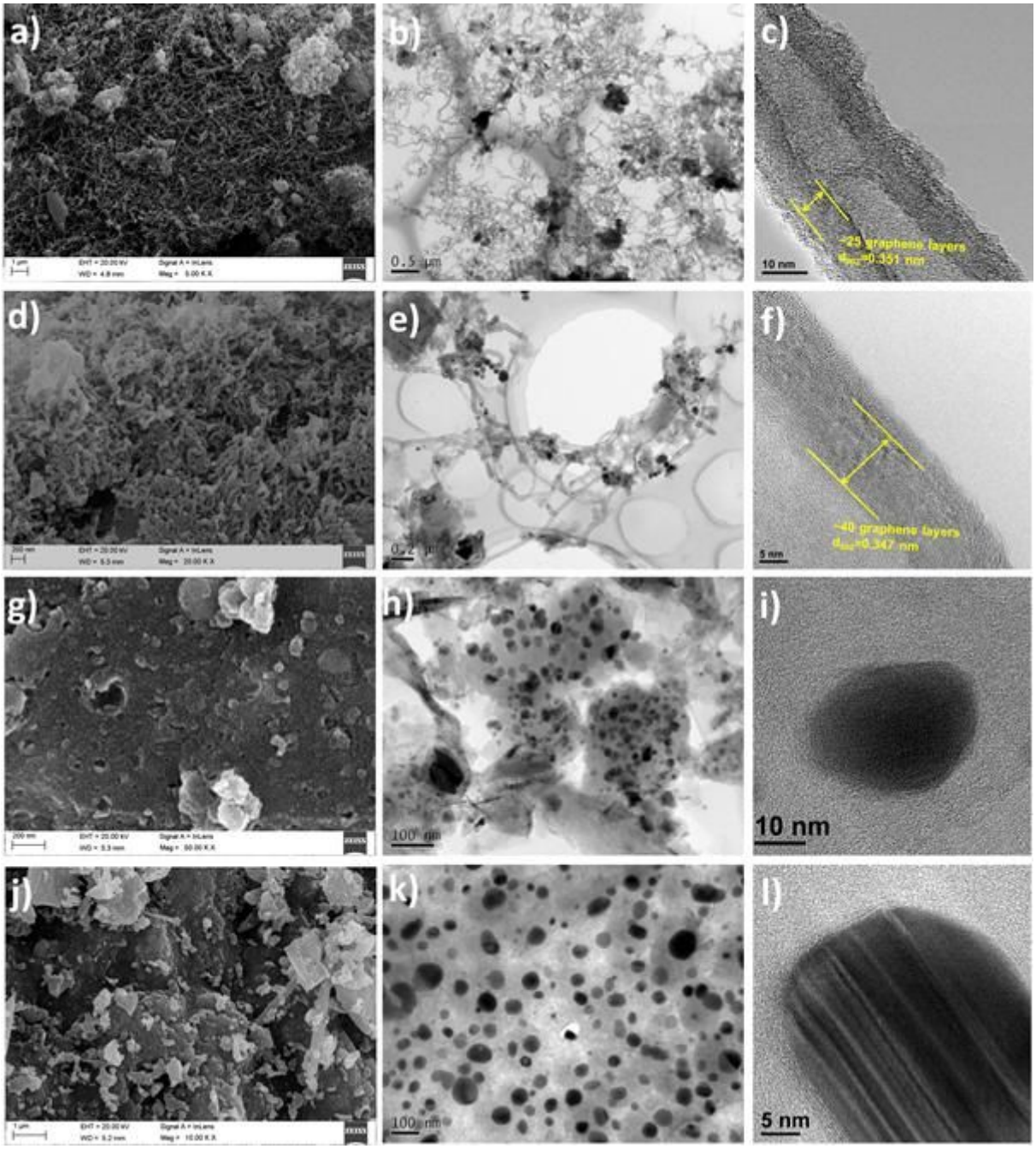


Figure 4

SEM (a, d, g, j), TEM (b, e, h, k) and HRTEM (c, f, i, l) images of the materials obtained through pyrolysis of MC (a-c), MN (d-f), MO (g-i) and MS (j-l).

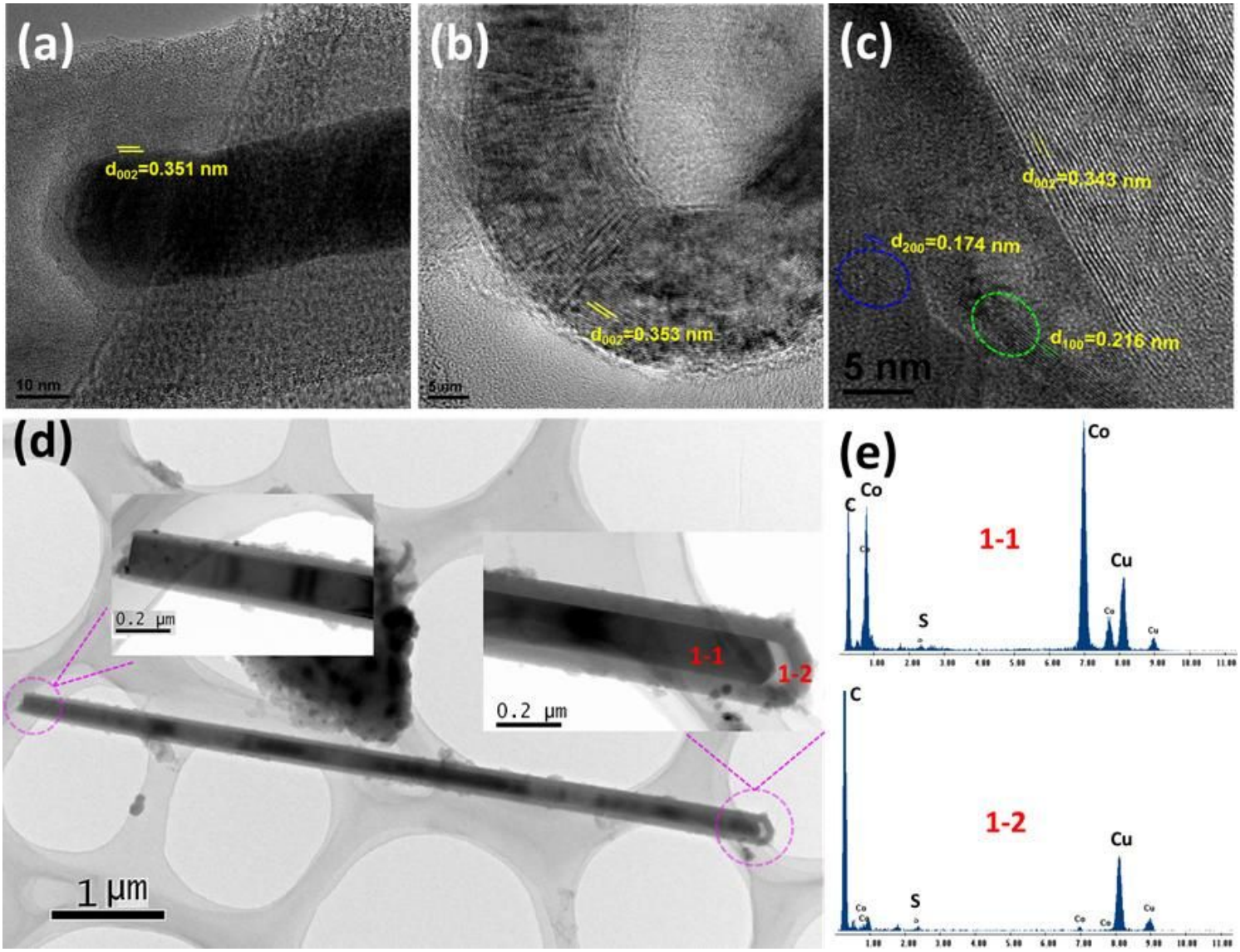


Figure 5

HRTEM images of the materials obtained through pyrolysis of MC (a) and MN (b) and MO (c). TEM images of the cobalt core/carbon sheath nanocable obtained through pyrolysis of MS (d), and its corresponding TEM-EDX spectra (e).

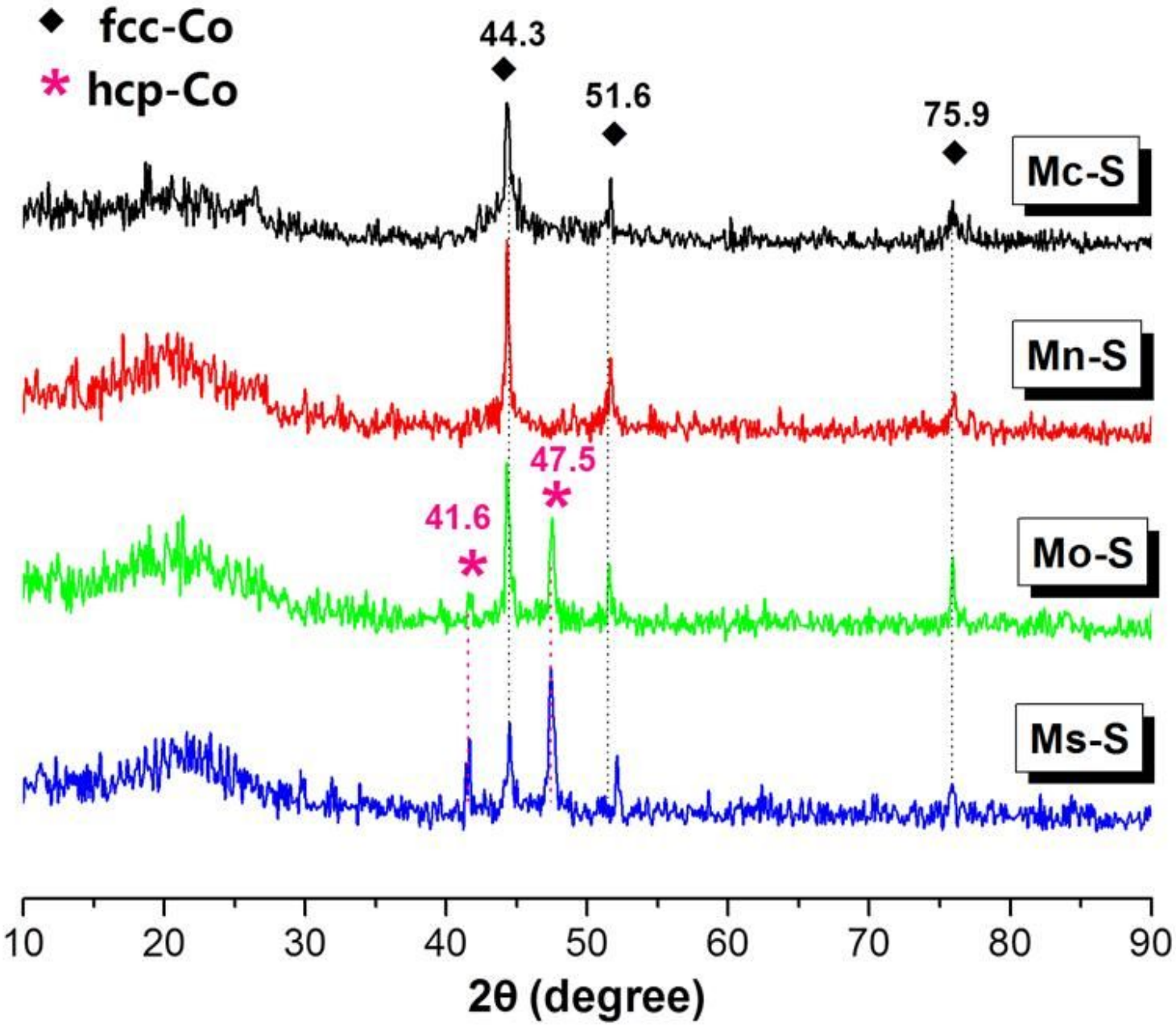


Figure 6

XRD diffractograms of MC-S, MN-S, MO-S and MS-S.

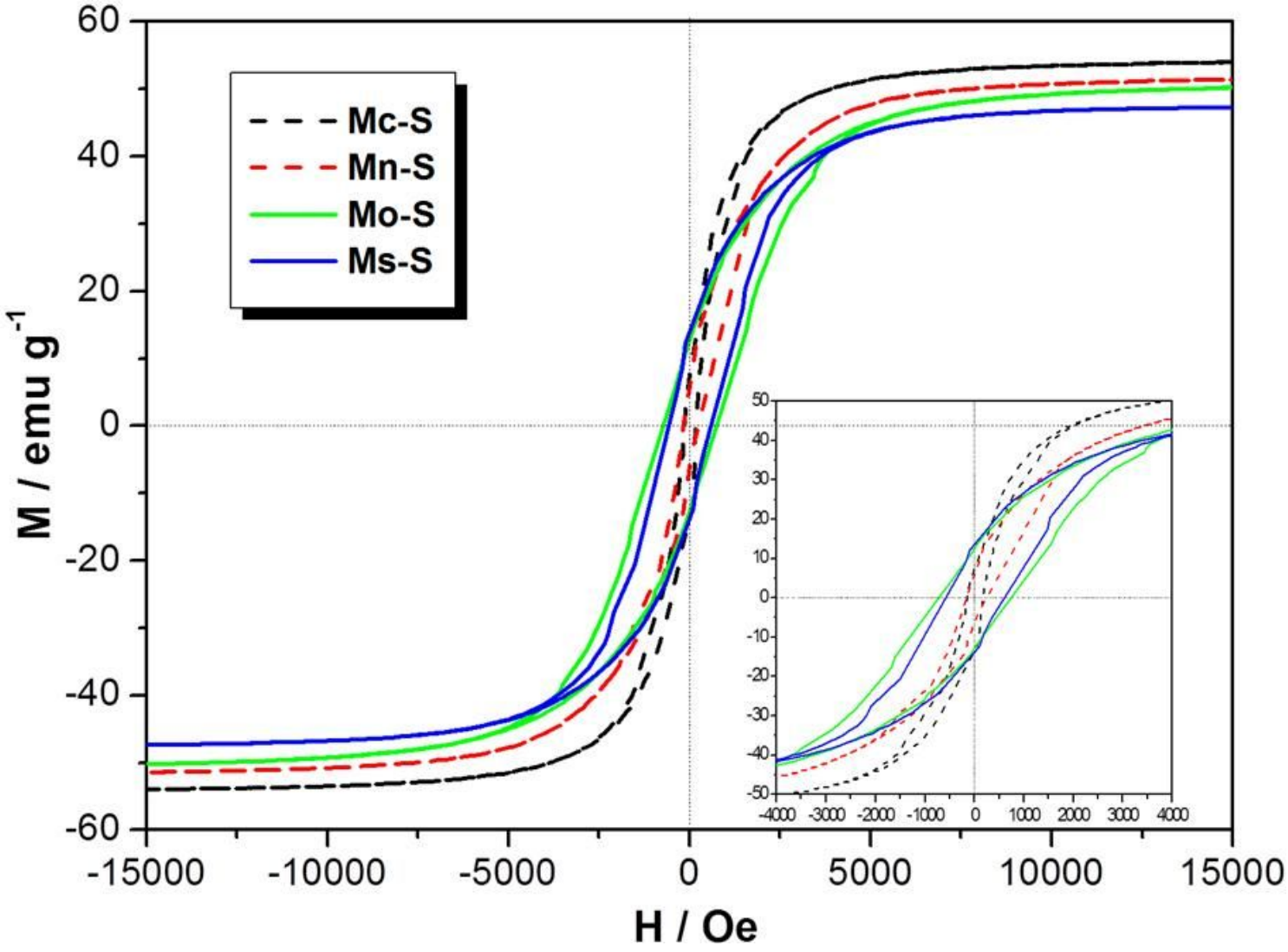


Figure 7

Plots of magnetization (M) versus applied magnetic field (H) at 300 K for MC-S, MN-S, MO-S and MS-S. Inset is enlarged portions of the M-H plot.

Supplementary Files

This is a list of supplementary files associated with this preprint. Click to download.

- SupportingInformation.pdf